Peer-reviewed version available at *Atoms* **2019**, *7*, 74; doi:10.3390/atoms7030074

Article

Temporally and Spatially Resolved Emission Spectroscopy of Cyanide, Hydrogen and Carbon in Laser-Induced Plasma

Christian G. Parigger [1],*, Christopher M. Helstern [1] and Ghaneshwar Gautam [2]

[1] Department of Physics and Astronomy, University of Tennessee/University of Tennessee Space Institute, 411 B. H. Goethert Parkway, Tullahoma, TN – 37388, USA; cparigge@tennessee.edu; chris.helstern@gmail.com
[2] Fort Peck Community College, 605 Indian Avenue, Poplar, MT 59255, USA; ggautam@fpcc.edu
* Correspondence: cparigge@tennessee.edu; Tel.: +1-931-841-5690

Abstract: This work examines atomic and molecular signatures in laser-induced plasma in standard ambient temperature and pressure environments, including background contributions to the spectra that depend on the laser pulse-width. Investigations include solids, gases, and nano-particles. Abel inversions of measured line-of-sight data reveal insight into the radial plasma distribution. For nominal 6 nanosecond laser pulses and for pulse-energies in the range of 100 to 800 mJ, expansion dynamics and turbulence due to shock phenomena are elucidated to address local equilibrium details that are frequently assumed in spatially averaged emission spectroscopy. Chemical equilibrium computations reveal temperature dependence of selected plasma species. Specific interests include atomic hydrogen (H) and cyanide (CN). Atomic hydrogen spectra indicate axisymmetric shell structures and isentropic expansion of the plasma kernel over and above the usual shockwave. The recombination radiation of CN emanates within the first 100 nanoseconds for laser-induced breakdown in a 1:1 CO_2:N_2 gas mixture when using nanosecond laser pulses to create the micro-plasma. The micro-plasma is generated using 1064 nm, 150 mJ, 6 ns Q-switched Nd:YAG laser radiation. Measurements of the optical emission spectra utilize a 0.64 m Czerny-Turner type spectrometer and an intensified charge-coupled device.

Keywords: Laser-induced plasma; atomic spectroscopy; molecular spectroscopy; cyanide; hydrogen; carbon

---

1. Introduction

Analysis of atomic species traditionally utilizes atomic emission spectroscopy of flames, plasmas, arcs, or sparks for quantification of elements in the sample. However, elemental composition studies frequently apply laser-induced breakdown spectroscopy (LIBS) in a variety of environments and with extensions to molecular characterizations of solids, liquids, and gases [1-4]. Investigations of laser-induced hydrogen plasmas serve the purpose of addressing fundamental aspects of time-resolved emission spectroscopy and associated dynamic processes following optical breakdown. Measurements of hydrogen plasmas allow one to determine important plasma parameters such as excitation electron density and temperature. Usually one measures the width of Balmer series lines of hydrogen that occur in the visible spectrum for electron density determination, and the integrated ratio of these lines or with respect to the continuum. Optical emission spectroscopy (OES) records indicate presence of molecular species that can elucidate sample composition or interaction processes in the ambient atmosphere [3-6]. Typically, atomic hydrogen lines, C_2 Swan bands and cyanide (CN) violet system show in various applications [6,7] of laser-induced OES such as in experiments with hydrocarbons [8]. Applications include laser ablation molecular isotope spectrometry [9], combustion analyses [10], and plant or medical diagnostics [11-13]. Detection methods of CN in the medical field include optical methods, electrochemical methods, mass- spectrometry, gas chromatography, and quartz crystal mass monitors [14]. These methods are adequate for detection of cyanide, yet molecular emission spectroscopy allows one to measure composition with a minimally invasive approach.

This work reports selected results from experiments using nanosecond laser spectroscopy of hydrogen plasma [15] and of CN molecular emission spectroscopy [16]. The CN recombination radiation occurs within the first 100 nanoseconds for laser-induced breakdown in 1:1 CO_2:N_2 gas mixtures. Aspects of the analysis include Abel inversions [17-21] and computational modeling [6] of the plasma. Analysis of asymmetric plasma expansion would require Radon inverse transformations [22]. Use of a chemical equilibrium code [23] allows one to predict species distribution as function of temperature and pressure and to investigate local thermodynamic equilibrium. Experiments with femtosecond laser pulses reveal advantages for laser ablation [12,13] with direct surface interaction LIBS, but without the type of laser-supported plasma encountered with nanosecond pulses.

2. Experimental details

The experimental arrangement consists of a set of components typical for time-resolved, laser-induced optical emission spectroscopy [14,15], or nanosecond laser-induced breakdown spectroscopy (LIBS). Primary instrumentations include a Q-switched Nd:YAG device (Quantel model Q-smart 850) that is operated at the fundamental wavelength of 1064-nm to produce full-width-at-half-maximum 6-ns laser radiation with an energy of 850 mJ per pulse, a laboratory type Czerny-Turner spectrometer (Jobin Yvon model HR 640) with a 0.64 m focal length and equipped with a 1200 grooves/mm grating, an intensified charge coupled device (Andor Technology model iStar DH334T-25U-03) for recording of temporally and spatially resolved spectral data, a laboratory chamber or cell with inlet and outlet ports together with a vacuum system, electronic components for synchronization, and various optical elements for beam shaping, steering, and focusing.

A singlet lens (Thorlabs model LA1509-C) accomplishes with f/5 focusing the generation of the optical breakdown micro-plasma in a chamber that contains the 1:1 CO_2:N_2 atmospheric gas mixture (Airgas ultra-high purity N_2 and research grade CO_2). Beam-splitters and apertures attenuate the energy/pulse from 850 to 150 mJ for the CN experiments. In air breakdown shadow-graph visualizations, a fused silica plano-convex lens (Thorlabs model LA4545) focuses the laser beam with f/10 optics. Figure 1 illustrates computed radial distributions [6] for the Thorlabs LA4545 lens for focusing with f/5 optics. The peak irradiance distributions are computed for 850 mJ, 6 ns, 1064 nm radiation. The tighter f/5 focusing reveals about one order of magnitude (or by a factor of 2^3) smaller focal volume than that obtained for f/10 focusing.

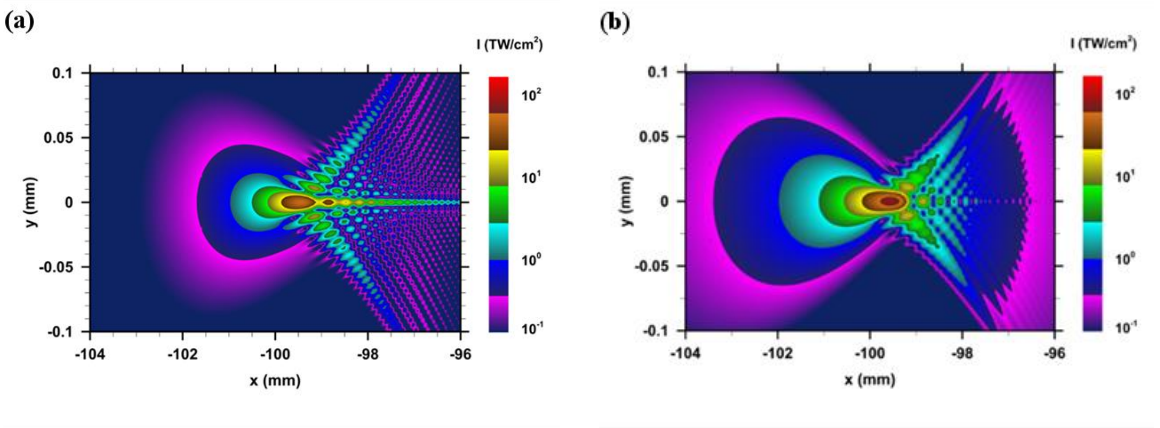

Figure 1. Spatial distribution of 1064-nm, **(a)** f/5, and **(b)** f/10 focusing with the Thorlabs LA4545, 100 mm focal length lens.

Peer-reviewed version available at Atoms 2019, 7, 74; doi:10.3390/atoms7030074

Captured shadow-graphs of the breakdown plasma serve the purpose of visualizing the plasma expansion [24]. Figure 2 illustrates typical shadowgraphs recorded in standard ambient temperature and pressure laboratory air. The figures reveal vertical stagnation layers that originate from multiple breakdown sites as indicated in the computed focal intensity distribution (see Fig. 1).

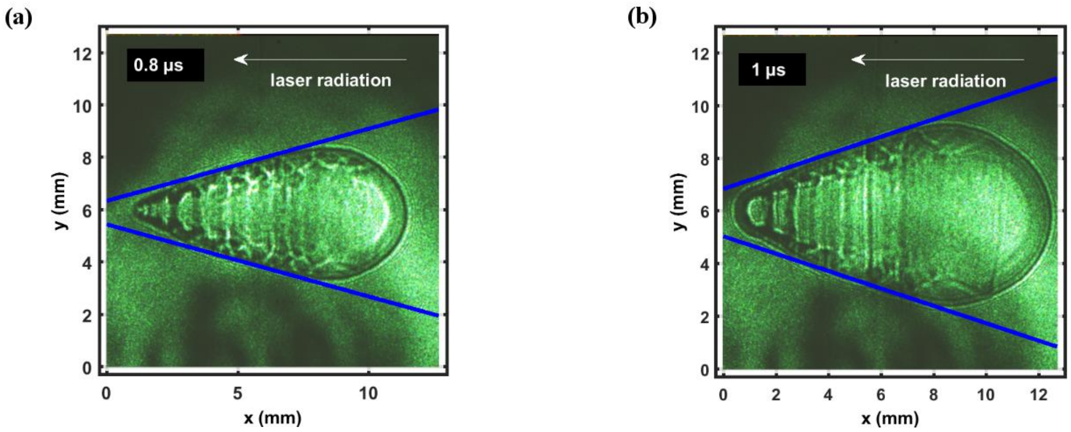

Figure 2. Plasma expansion **(a)** at 0.8 μs **(b)** at 1 μs. At 1 μs time delay, the plasma expands vertically at ~ Mach 3 (~1 km/s). The slopes in **(a)** and **(b)** are ± 3.6 and ± 3, respectively, indicate the forward envelopes of the shock waves.

The laser-supported plasma expansion is consistent with previous focal volume investigations [25] and with the Taylor-Sedov blast-wave model [26,27]. Increased electron density and temperature occur in the outer region of the plasma kernel as evidenced by the bright-to-dark boundaries that appear to cause multiple reflection inside the shock wave. The vertical extend is about a factor of 1.4 smaller for 150 mJ pulses than that for 850 mJ pulses, according to the Taylor-Sedov energy dependency for the radius of a spherical expansion.

4. Results and discussion

The experimental series for the separate measurements of atomic H and CN molecular distribution after optical breakdown includes evacuating the cell to a nominal mercury pump vacuum of 10^{-4} Pa (10^{-6} Torr) and then introducing hydrogen or the N_2 : CO_2 mixture. Figure 3 illustrates typical raw images of captured time-resolved data following optical breakdown [16] in the ultra-high pure N_2 and research grade CO_2.

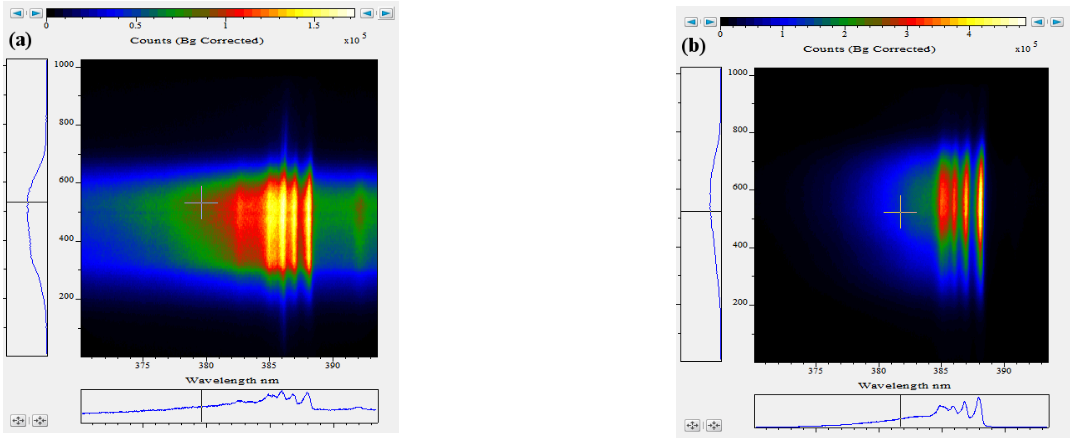

Figure 3. Raw spectra **(a)** 0.45 μs and **(b)** 3.7 μs after optical breakdown in a 1:1 CO_2:N_2 atmospheric gas mixture.

Peer-reviewed version available at Atoms 2019, 7, 74; doi:10.3390/atoms7030074

In the reported investigations, signatures of the 0-0, 1-1, 2-2, 3-3, 4-4 band heads begin to emanate for time delays of the order of 0.1 µs from optical breakdown. Moreover, the plasma typically propagates towards the laser side. The recorded data indicate a ~ 0.8 mm upward CN-signal propagation in the 370 to 393.5 nm spectral, 7 mm object window during the first 5 µs, from a delay of 0.2 µs to 5.2 µs. Optical breakdown inside the chamber occurs at a rate of 10 Hz, with the laser beam focused with f/5 optics from the top, or parallel to the slit. The detector pixels are binned in 4 tracks along the slit direction, resulting in obtaining 256 spectra for each time delay. Figure 3 shows accumulated raw data from 100 consecutive optical breakdown events, recorded at a time delay of 0.450 µs and a gate width of 0.125 µs. The vertical axis indicates the slit-height, the laser beam is focused from the top. With 1:2 imaging, and a pixel resolution of 13.6 µm, the discernable plasma size in the cell amounts to ~ 3 mm. The figure illustrates that the CN band heads of the $\Delta v = 0$ sequence are well-developed, and it also displays an atomic line near 386.2 nm that is the carbon C I 193.09-nm atomic line, recorded in second order [16].

Abel inverse transformation allows one to obtain the radial distribution of the plasma. Strictly speaking, radially symmetric profiles are required for Abel inversion. Analysis of the molecular CN spectra utilizes the same methods as previously applied for atomic hydrogen spectra [17,18]. The integral equation describes line-of-sight averaging,

$$\mathrm{I}(z,\lambda) = 2\int_z^{\rho} \mathrm{I}(r,\lambda)\frac{r}{\sqrt{r^2-z^2}}\,dr\,. \qquad (1)$$

The measured, line-of sight data, $\mathrm{I}(z,\lambda)$, along the slit dimension, z, are inverted for each wavelength, λ, to obtain the volumetric radial distribution, $\mathrm{I}(r,\lambda)$, with the upper limit much larger, $\varrho \gg R$, than the radius, R, of the plasma. The choice of the number of Chebyshev polynomials for the inversion [17] is equivalent to the use of a digital filter [18] that causes broadening of computed radial spectra. In this work, the inversion uses 10 polynomials, a smaller number of polynomials would cause smaller spectral resolution.

Figure 4 displays results of Abel-inverted hydrogen data for a time delay of 0.4 µs from optical breakdown. For the recorded data, the constructed Boltzmann plots utilize H_α, H_β, and H_γ integrated line shapes to provide a measure for the excitation temperature distribution [15]. Figure 4 portrays a cooler central region and a relatively hot ring of the order of 100,000 K (8.6 eV). As indicated in the figure, the kernel expands at or near the speed of sound in hydrogen gas.

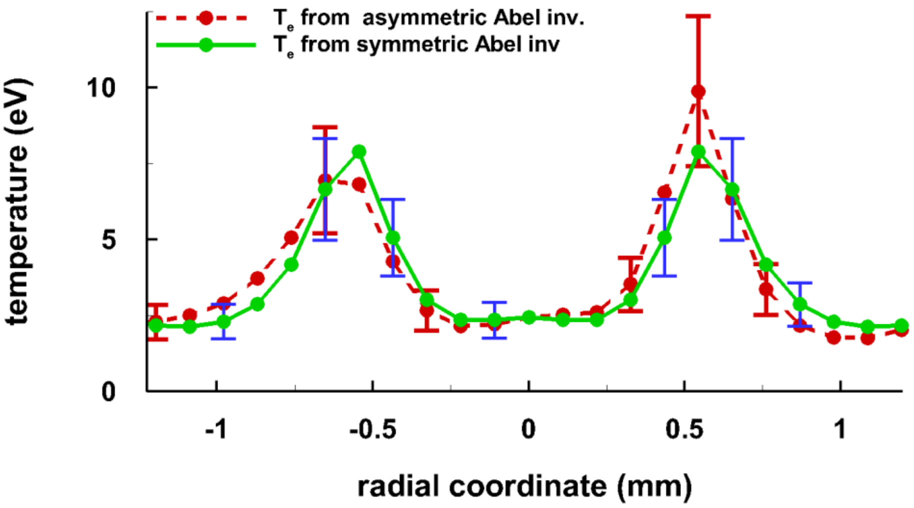

Figure 4. Electron temperature, T_e, vs. radial position.

Peer-reviewed version available at *Atoms* **2019**, *7*, 74; doi:10.3390/atoms7030074

Figure 5 shows the corresponding electron densities [15,19,20]. The error bars are in part due to the lower fidelity of the Abel inversion for a time delay of 0.4 μs. Wavelength and detector system-sensitivity calibrated CN spectral data are Abel inverted [16].

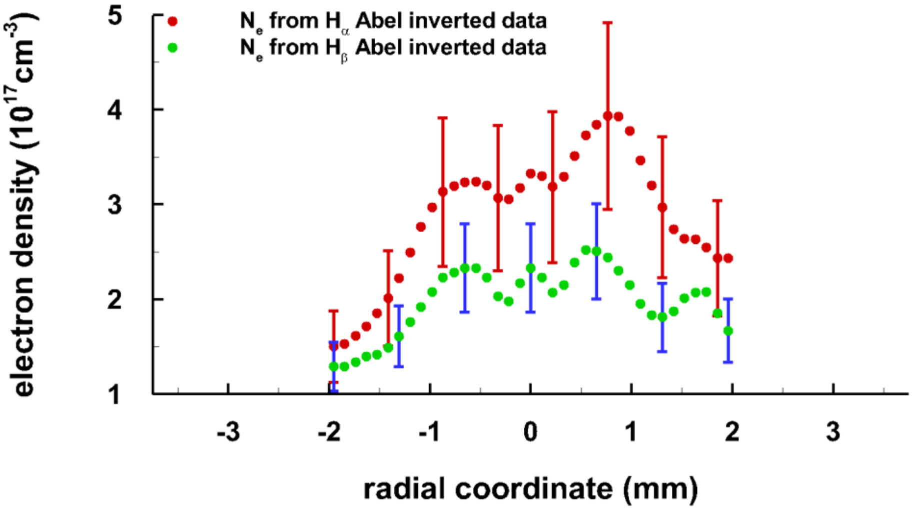

Figure 5. Electron density, n_e, vs. radial position.

Figure 6 displays the results and it shows a comparison of computed and of measured spectra [28,29]. Analogous to recently reported hydrogen nitrogen gaseous mixtures [30], the CN signals are weaker at the center and indicate a slightly lower temperature than for the 0.85 mm position. There appears to be residual interference from an atomic line at 386.2 nm that indicates the carbon line at 193.09-nm line [20,21], measured in second order.

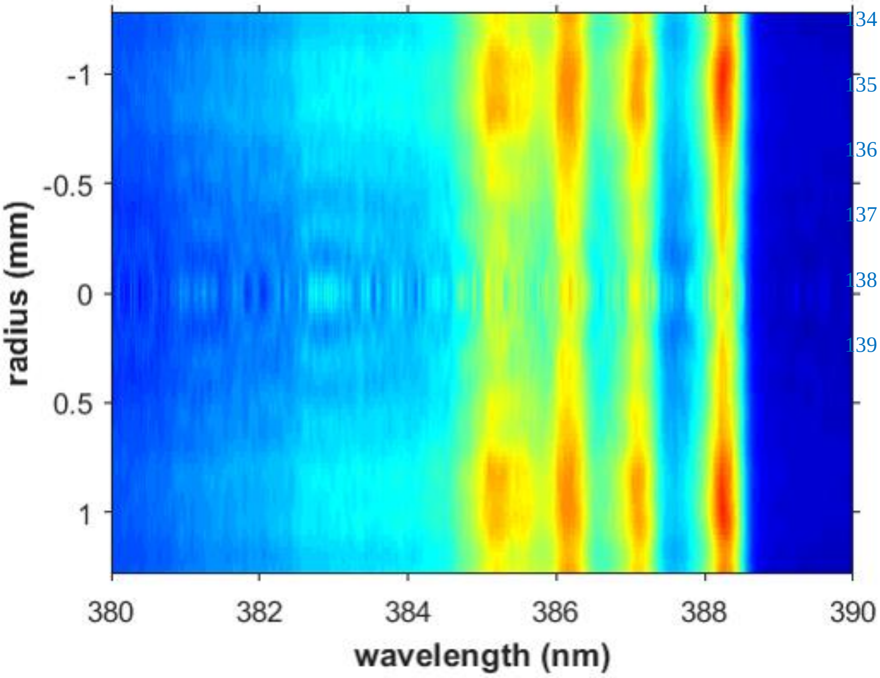

Figure 6. Abel inverted spectra versus radius at 1.2-μs time delay, gate 0.125 μs.

Peer-reviewed version available at *Atoms* **2019**, *7*, 74; doi:10.3390/atoms7030074

Figure 7 illustrates measured and fitted CN spectra at the radius of 0.85 mm, indicating a fitted FWHM of 0.45 nm and a temperature of 8.6 kK. For comparison, reasonable signal to noise spectra at 1 mm and at a delay of 3.7 μs, reveal expected lower temperature than that for the 1.2 μs time delay.

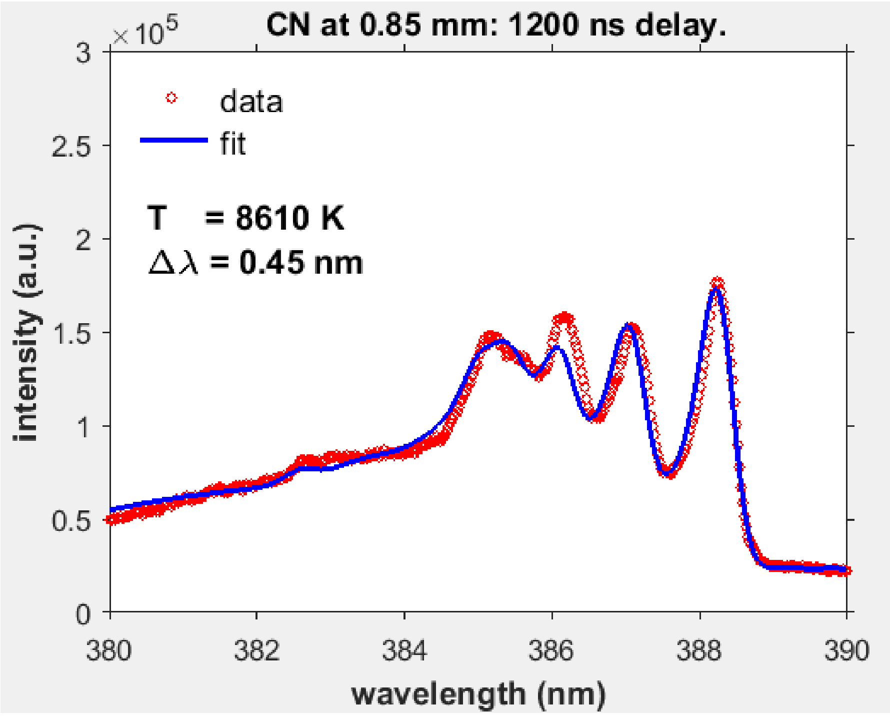

Figure 7. Inferred CN excitation temperature at the radius of 0.85 mm.

One would expect that the CN molecule distribution is close to uniform in chemical equilibrium. For time delays in the range of 5 to 50 μs, the line-of-sight molecular CN spectra are well developed, and the recorded optical emissions originate from a decreasing volume with increasing gate delay. In addition, CN recombination radiation signals may be stronger for specific ranges of temperature. Computation of the freely available Chemical Equilibrium with Applications (CEA) code [23] elucidate CN mass fractions versus temperature. Several atoms and molecules including ionic species are part of the CEA computations, but the results for the CN mass fractions are of primary interest in this work. Figure 8 shows the CN distribution for both air and the mixture as function of temperature.

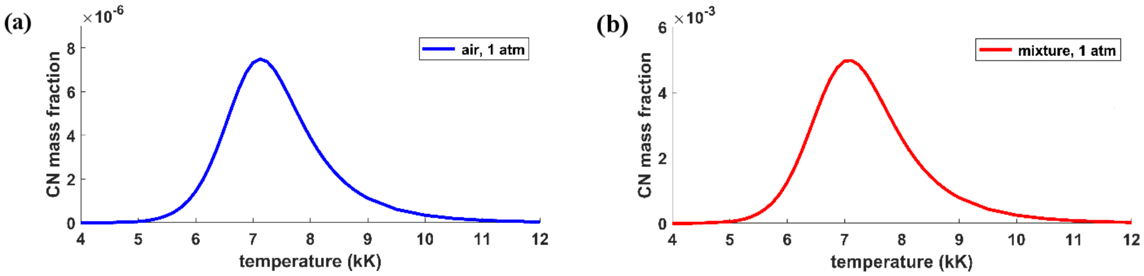

Figure 8. CN **(a)** air and **(b)** mixture mass fraction vs. temperature in chemical equilibrium, CN shows a maximum near 7 kK for the 1:1 atmospheric CO_2:N_2 mixture. CN fractions in air are nearly 3 orders of magnitude lower than that for the mixture.

Peer-reviewed version available at *Atoms* **2019**, *7*, 74; doi:10.3390/atoms7030074

The recombination signals from the mixture are strongest near 7 kK. Using the tabulated chemical equilibrium results [23] at a temperature of 7 kK, one finds that the number of CN molecules in the mixture and air amount to ~ 3×10^{15} cm^{-3} and ~ $5\times1\ 0^{12}$ cm^{-3}, respectively. Spectra analyses of the central region data at 0.45-μs time delay indicate slightly lower temperatures at center than that obtained at a radial position of 1 mm, and spectroscopic interference from th e likely carbon line in 2nd order is apparent for time delays of 0.45 and 1.2 μs. Line-of-sight data consist of average spectra with contributions from regions at different temperatures. For instance, the molecular CN spectra near the plasma edges, viz. near the top and bottom of the spectra (see Figure 3) show smaller signals but reveal higher temperatures than in the center portion.

5. Conclusions

Measured hydrogen and cyanide recombination spectra indicate a spherical shell structure of the plasma kernel inside the shock wave early in the plasma decay. For hydrogen, electron density and excitation temperature are higher in the peripheral region than near the center due to expansion dynamics of the plasma kernel after optical breakdown. The recombination radiation from CN shows a similar trend for early time delays, namely, higher excitation temperatures occur in the outer region than near the center of the plasma kernel. Strictly speaking, the application of Abel inversion requires a symmetric light source, yet the analysis of the extent of asymmetry in the hydrogen plasma leads to variations within the estimated error bars. Shadow-graph studies in air would support symmetrizing the spectral data recorded in the CO_2:N_2 mixture and applying Abel inverse transforms to extract the spatial variation of the CN optical emission signals.

Funding: The authors appreciate the support in part by the Center for Laser Application, a State of Tennessee funded Accomplished Center of Excellence at the University of Tennessee Space Institute.

Author Contributions: Christian G. Parigger conceived and performed the experiments with Ghaneshwar Gautam. Christian G. Parigger analyzed the result together with Christopher M. Helstern, and all authors contributed to the writing of the article.

Conflicts of Interest: The authors declare no conflict of interest.

References

[1] Cremers, D.A.; Radziemski, L.J. *Handbook of Laser-Induced Breakdown Spectroscopy*; Wiley & Sons Ltd.: USA, **2006**.

[2] Singh, J.P.; Thakur, S.N. (Eds.); *Laser Induced Breakdown Spectroscopy*; Elsevier: NL, **2007**.

[3] Hahn, D.W.; Omenetto, N. Laser-Induced Breakdown Spectroscopy (LIBS), Part I: Review of Basic Diagnostics and Plasma-Particle Interactions: Still-Challenging Issues within the Analytical Plasma Community. *Appl. Spectrosc.* **2010**, *64*, 335A – 336A.

[4] Hahn, D.W.; Omenetto, N. Laser-Induced Breakdown Spectroscopy (LIBS), Part II: Review of Instrumental and Methodological Approaches to Material Analysis and Applications to Different Fields *Appl. Spectrosc.* **2012**, *66*, 347 – 419.

[5] Parigger, C.G; Surmick, D.M.; G. Gautam, G.; EL Sherbini, A.M. Hydrogen alpha laser ablation plasma diagnostic. *Opt. Lett.* **2015**, *40*, 3436 – 3439.

[6] Parigger, C.G. Laser-induced breakdown in gases: experiments and simulation; Chapter 4 in: A.W. Miziolek, V. Palleschi, I. Schechter (Eds.), *Laser Induced Breakdown Spectroscopy*; Cambridge University Press: USA, **2006**.

Peer-reviewed version available at Atoms 2019, 7, 74; doi:10.3390/atoms7030074

[7] Dong, M.; Lu, J.; Yao, S.; Zhong, Z.; Li, Junyan; Li, Jun; Lu, W. Experimental study on the characteristics of molecular emission spectroscopy for the analysis of solid materials containing C and N. *Opt. Express* **2011**, *19*, 17021 – 17029.

[8] Parigger, C.G.; Dackman, M.; Hornkohl, J.O.Time-resolved spectroscopy measurements of hydrogen-alpha, -beta, and -gamma emissions. *Appl. Opt.* **2008**, *47*, G1 – G6.

[9] Dong, M.; Chan G.C.-Y., X. Mao, X.; Gonzalez, J.J.; J. Lu, Russo, R.E. Elucidation of C_2 and CN formation mechanisms in laser-induced plasmas through correlation analysis of carbon isotopic ratio. *Spectrochim. Acta Part B: At. Spectrosc.* **2014**, *100*, 62 – 69.

[10] Kotzagianni, M.; Couris, S. Femtosecond laser induced breakdown spectroscopy of air–methane mixtures. *Chem. Phys. Lett.* 2013, *561 – 562*, 36 – 41.

[11] Minorsky, P.V. On the Inside. *Plant Physiol.* **2011**, *155*, 169 – 170.

[12] Baudelet, M.; Guyon, L.; Yu, J.; Wolf, J.-P.; Amodeo, T.; Fréjafon, E.; Laloi, P. Spectral signature of native CN bonds for bacterium detection and identification using femtosecond laser-induced breakdown spectroscopy. *J. Appl. Phys*. **2006**, *88*, 063901.

[13] Baudelet, M.; Guyon, L.; Yu, J.; Wolf, J.-P.; Amodeo, T.; Fréjafon, E.; Laloi, P. Femtosecond time-resolved laser-induced breakdown spectroscopy for detection and identification of bacteria: A comparison to the nanosecond regime. *J. Appl. Phys*. **2006**, *99*, 084701.

[14] Ma, J.; Dasgupta, P.L. Recent developments in cyanide detection: a review. *Anal. Chim. Acta* **2010**, *673*, 117 – 125.

[15] Parigger, C.G.; Surmick, D.M.; Gautam, G. Self-absorption characteristics of measured laser-induced plasma line shapes. *J. Phys.: Conf. Ser.* **2017**, *810*, 012012.

[16] Parigger, C.G.; Helstern, C.M; Gautam, G. Molecular emission spectroscopy of cyanide in laser-induced plasma. *Int. Rev. At. Mol. Phys.* **2017**, *8*, 25 – 35.

[17] G. Pretzler. A New Method for Numerical Abel-Inversion. *Z. Naturforsch.* **1991**, *46a*, 639 – 641.

[18] G. Pretzler, H. Jäger, T. Neger, H. Philipp, and J. Woisetschläger. Comparison of Different Methods of Abel Inversion Using Computer Simulated and Experimental Side-On Data. *Z. Naturforsch.* **1992**, *47a*, 955.

[19] Parigger, C.G.; Gautam, G.; Surmick, D.M. Radial electron density measurements in laser-induced plasma from Abel inverted hydrogen Balmer beta line profiles. *Int. Rev. At. Mol. Phys. 2015*, *6*, 43 – 55.

[20] Helstern, C.M.; Parigger, C.G. Time-resolved plasma spectroscopy of diatomic molecular cyanide, J. Phys.: Conf. Ser. **2019**, in press.

[21] Parigger, C.G; Surmick, D.M.; Helstern, C.M.; Gautam, G.; Bol'shakov. A.A. Molecular Laser-Induced Breakdown Spectroscopy; Chapter 7 in: J.P. Singh, S.N. Thakur (Eds.); *Laser Induced Breakdown Spectroscopy*; Elsevier: NL, **2019**, in press.

[22] Eschlböck-Fuchs, S.; Demidov, A.; Gornushkin, I.; Schmid, T.; Rössler, R.; Huber, N.; Panne, U.; Pedarnig, J. Tomography of homogenized laser-induced plasma by Radon transform technique. *Spectrochim. Acta Part B: At. Spectrosc.* **2016**, *123*, 59 – 67.

[23] McBride B.J.; Gordon, S. *Computer Program for Calculating and Fitting Thermodynamic Functions*, NASA RP-1271, 1992; on-line 2005 version at https://cearun.grc.nasa.gov/ (last accessed November 26, 2017).

[24] Gautam, G.; Helstern, C.M.; Drake, K.A.; Parigger, C.G. Imaging of Laser-induced Plasma Expansion Dynamics in Ambient Air. *Int. Rev. At. Mol. Phys.* **2016**, **7**, 45 – 51.

[25] Chen, Y.-L.; Lewis, J.W.L.; C. Parigger, C.G. Spatial and Temporal Profiles of Pulsed Laser-Induced Air Plasma Emissions. *J. Quant. Spectrosc. Radiat. Transf.* **2000**, *67*, 91 – 103.

[26] Taylor, G. The Formation of a Blast Wave by a Very Intense Explosion. II. The Atomic Explosion of 1945. *Proc. Roy. Soc. A* **1950**, *201*, 175 – 186.

[27] Campanella, B.; Legnaioli, S.; Pagnotta, S.; Poggialini, F.; Palleschi, V. Shock Waves in Laser-Induced Plasmas. *Atoms* **2019**, *7*, 7020057.

[28] Hornkohl, J.O.; Parigger, C.G.; Lewis, J.W.L. Temperature Measurements from CN Spectra in a Laser-Induced Plasma. *J. Quant. Spectrosc. Radiat. Transf.* **1991**, *46*, 405 – 411.

[29] Parigger, C.G.; Woods, A.C.; Surmick, D.M.; Gautam, G.; Witte, M.J.; Hornkohl, J.O. Computation of diatomic molecular spectra for selected transitions of aluminum monoxide, cyanide, diatomic carbon, and titanium monoxide. *Spectrochim. Acta Part B* **2015**, *107*, 132 – 138.

[30] Gautam. G.; Parigger, C.G.; Helstern, C.M.; Drake, K.A. Emission Spectroscopy of Expanding Laser-Induced Gaseous Hydrogen-Nitrogen Plasma. *Appl. Opt.* **2017**, *33*, 9277 – 9284.